Impact of Aliovalent Alkaline-Earth Metal Solutes on Ceria Grain Boundaries: A Density Functional Theory Study

Tara M. Boland^a, Peter Rez^b, Peter A. Crozier^a, Arunima K. Singh^{b,*}

 ^aSchool for Engineering of Matter, Transport and Energy, Arizona State University, Tempe, AZ, USA
 ^bDepartment of Physics, Arizona State University, Tempe, AZ, USA

Abstract

Ceria has proven to be an excellent ion-transport and ion-exchange material when used in polycrystalline form and with a high-concentration of aliovalent doped cations. Despite its widespread application, the impact of atomic-scale defects in this material are scarcely studied and poorly understood. In this article, using first-principles simulations, we provide a fundamental understanding of the atomic-structure, thermodynamic and electronic properties of undoped grain-boundaries (GBs) and alkaline-earth metal (AEM) doped GBs in ceria. Using density-functional theory simulations, with a GGA+U functional, we find the $\Sigma 3 (111)/[\bar{1}01]$ GB is energetically more stable than the $\Sigma 3 (121)/[\bar{1}01]$ GB due to the larger atomic coherency in the $\Sigma 3$ (111)/[$\bar{1}01$] GB plane. We dope the GBs with $\sim 20\%$ [M]_{GB} (M=Be, Mg, Ca, Sr, and Ba) and find that the GB energies have a parabolic dependence on the size of solutes, the interfacial strain and the packing density of the GB. We see a stabilization of the GBs upon Ca, Sr and Ba doping whereas Be and Mg render them energetically unstable. The electronic density of states reveal that no defect states are present in or above the band gap of the AEM doped ceria, which is highly conducive to maintain low electronic mobility in this ionic conductor. The electronic properties, unlike the energetic properties, exhibit complex inter-dependence on the structure and

Email address: arunimasingh@asu.edu (Arunima K. Singh)

^{*}Corresponding author

chemistry of the host and the solutes. This work makes advances in the atomic-scale understanding of aliovalent cation doped ceria GBs serving as an anchor to future studies that can focus on understanding and improving ionic-transport.

Keywords: Ceria, Grain-Boundaries, Aliovalent Dopants

1. Introduction

Doped polycrystalline electroceramic oxides are an important class of materials in which point defects in the bulk and grain boundaries play a key role in regulating mechanical, optical, thermal, magnetic, catalytic and charge transport properties [1, 2, 3, 4, 5, 6, 7, 8, 9, 10]. The transport and ion exchange functionalities of electroceramics make them suitable for many technological applications including catalysts [11, 12], solid electrolytes and electrodes [13, 14, 15], gas separation membranes [16, 17], gas sensing systems [18], and memristors [19]. Many of the relevant oxides have fluorite or perovskite structures where oxygen transport occurs via thermally activated vacancy hopping and electron transport takes place via polaron hopping. In these oxides, aliovalent cation doping can be employed to introduce oxygen vacancies, manipulate oxygen migration energies, and regulate the concentration of mobile electrons and holes.

Many applications employ polycrystalline solids where the overall properties of the material are significantly impacted by the presence of grain boundaries. For example, oxygen ionic conductivity is degraded by grain boundaries that block oxygen transport [20, 21, 22, 23, 24, 25, 26] and it is commonly assumed that there is a high concentration of immobile positively charged oxygen vacancies at the GB core which repel mobile vacancies. There is a growing body of experimental evidence [27, 2, 3, 28, 29, 30, 5, 6, 31] and theoretical predictions [29, 30, 32] that confirm that aliovalent solute segregate to the GBs will significantly impact many of the physio-chemical properties. These observations are not surprising considering the typical temperatures employed for ceramic processing of polycrystalline electrolytes. There is a strong driving force for solute segregation to reduce the overall system energy due to cation

size mismatch, electrostatic forces (i.e. GB core charge neutralization), and/or reduction in the GB energy. [27, 28, 33, 32, 9] Often, GB solute concentrations are present in higher concentrations than the bulk solubility limits without precipitation of a second phase. [34, 7, 10, 31, 35] The ionic conductivity behavior of GBs with high solute concentration is substantially enhanced contradicting the predictions of the dilute-solute space charge models. [7, 10] The origin for the conductivity increase is not currently understood and requires a fundamental investigation of the role of solutes on the atomic structure and bonding at grain boundaries.

In this article, using first-principles simulations, we provide a fundamental understanding of the atomic-structure, stability and electronic properties of pristine as well as aliovalent, alkaline-earth metal (AEM) doped GBs in CeO₂. We show that a local doping with $\sim 20\%$ [M]_{GB} (M=Be, Mg, Ca, Sr, and Ba) has a significant impact on the energetic stability of the GBs. Using densityfunctional theory simulations with a GGA+U functional we examine the structure, energetic stability and coordination of atoms at the GB interface for two of the more frequently observed grain-boundaries in Ca-doped ceria, [36, 7] the $\Sigma 3 (111)/[\bar{1}01]$ and $\Sigma 3 (121)/[\bar{1}01]$ GB. We show that a local doping with $\sim 20\%$ $[M]_{GB}$ (M=Be, Mg, Ca, Sr, and Ba) has a significant impact on the energetic stability of the GBs. Element-projected and orbital-projected density of states show that no defect states are present in or above the band gap of the AEM doped ceria, which is conducive to maintaining lower electronic mobilities that is necessary for good ionic transport. In addition, we find that the band gap of ceria can be modulated by up to 0.3 eV by selecting different AEM dopants at the ceria GB.

2. Computational Methods

All simulations are based on density functional theory (DFT) using the projector augmented wave method [37, 38] as implemented in the plane-wave code VASP. [39, 40, 41, 42] All simulations included spin-polarization and the

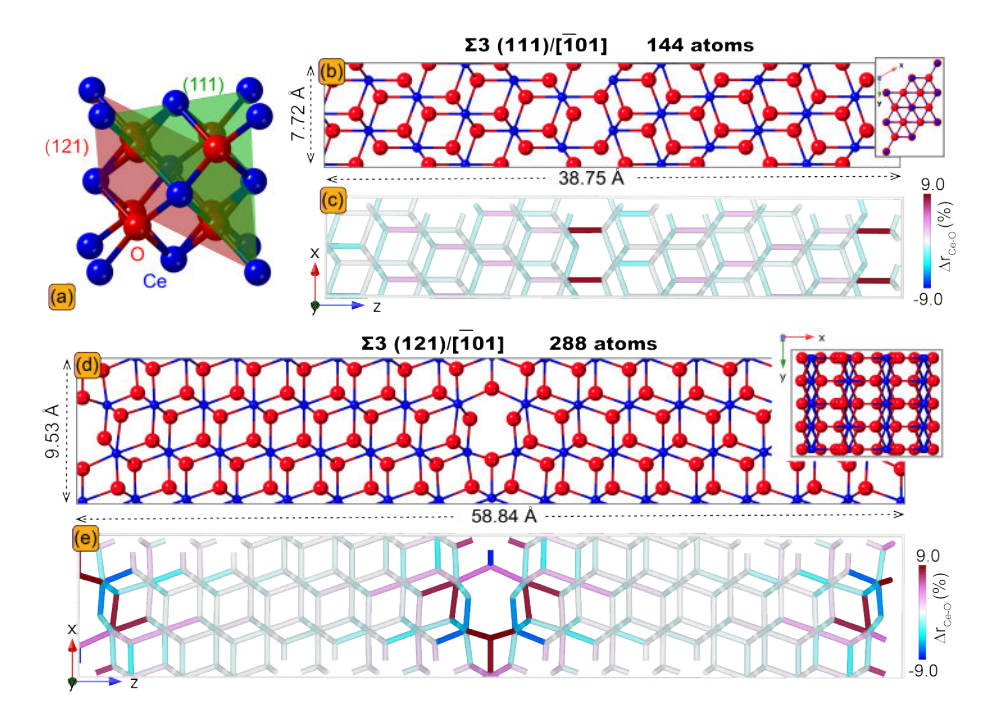


Figure 1: (a) Structure of the conventional fluorite CeO₂ unit cell. The (121) and (111) lattice planes are shown as shaded planes. These indicate the interface planes for the GBs. (b) The xz-plane of the $\Sigma 3$ (111)/[$\bar{1}01$] GB supercell. Inset shows the GB structure from the GB containing plane, i.e., the x-y plane where the GB is located in the center of the plane. (c) The percent deviation of the bonds in the $\Sigma 3$ (111)/[$\bar{1}01$] GB supercell from the average Ce-O bond length of the GB supercell, $\Delta r_{\rm Ce-O}$, is shown as a color map. Blue indicates compressed bonds while red indicates tensile bonds. (d) The xz-plane of the $\Sigma 3$ (121)/[$\bar{1}01$] GB supercell. Inset shows the structure from the x-y plane. (e) $\Delta r_{\rm Ce-O}$ is shown as a color map.

generalized gradient approximation (GGA) with the Perdew-Burke-Ernzerhof (PBE) [43, 44] exchange-correlation functional was used. In addition, the strong correlation effects of the Ce 4f electrons were treated within GGA using the Hubbard U correction (GGA+U) formulated by Dudarev et. al. [45]. An on-site Coulomb interaction, $U_{eff} = 5$ eV, was used for Ce, as determined by Dholabhai et al. [46] as well as many others [47, 48, 49, 50], to provide a better fit with the experimental band gap ($E_{\rm gap}$), lattice parameter (a_0), and bulk modulus (B_0) compared to traditional GGA methods. For a 2x2x2 supercell of bulk ceria, we find that $E_{\rm gap}[{\rm O}(2p) \rightarrow {\rm Ce}(4f)] = 2.0$ eV, $a_0 = 5.494$ Å, and $a_0 = 180.59$ GPa and the corresponding experimentally measured values are $E_{\rm gap}[{\rm O}(2p) \rightarrow {\rm Ce}(4f)] = 3$ eV [51], $a_0 = 5.411$ Å [52], and $a_0 = 204-236$ GPa. [53, 51] The chosen value of $a_0 = 204-236$ GPa atoms—unlike traditional GGA which results in delocalized electrons on all cerium ions in the lattice.

For ceria, standard DFT fails to describe the insulating behavior and the use of the Hubbard (U) parameter that prioritizes electron localization on the nearby Ce 4f states is essential to correct for this. This electron localization is well established in the experimental literature that characterize so many processes in ceria based systems. [11] The DFT treatment of ceria is well established within the GGA+U method and typically overestimates the lattice parameters with errors of 1%-2%. [54] Our computed lattice parameter value is overestimated by 1.53%, well within the expected accuracy of the DFT method as well as recently published literature. [48, 47, 55]

Band gap underestimation within DFT is also a well-established trend [56, 57, 58] that can produce discrepancies upwards of 1-2 eV [58] or a 40%-50% difference between calculation and experimental measurements [59] dependent upon the class of the material. However, this is a systematic error present in all calculations due to the band gap underestimation error [60, 56, 58] and the choice of the exchange-correlation functional. [61, 62, 63] Due to this systematic error, although absolute band gap energies might not agree with experimental measurement, differences from structural changes follow trends expected from

experimental measurements. The values of U, our lattice parameter and band gap are shown in SI Table 2 for comparison with other GGA+U calculations. [48, 47, 50, 49, 55]

Note that, for our chosen simulation parameters, the maximum numerical error present in the band gap energy is at most \pm 0.1 eV [64].

A plane wave cutoff energy of 400 eV was used for all cases except for the volume optimization of ceria, where it was set to 520 eV. This cutoff energy was sufficient to converge the forces [65] acting on each ion to 0.01 eV Å/atom or better. A block Davidson [66] minimization algorithm was used to achieve a convergence in total energy per cell on the order of 0.001 eV or better.

Figure 1b and Figure 1d show the $\Sigma 3 (111)/[\bar{1}01]$ and $\Sigma 3 (121)/[\bar{1}01]$ GBs, respectively. These were constructed from the conventional fluorite unit cell of CeO₂, Figure 1a, using pymatgen [67]—an open-source Python library for materials analysis. The large variation in the atomic structures of these GBs and the presence of high-quality experimental GB character and compositional characterization of GBs in polycrystalline Ca-doped ceria via electron backscattered diffraction and transmission electron microscopy [36, 7] motivates the choice of these two GBs for this study. Furthermore, the atomic structure for the $\Sigma 3 (111)/[\bar{1}01]$ GB has been experimentally confirmed by Feng et. al. [68]. Our computationally considered CeO_2 $\Sigma 3$ (111)/ $[\bar{1}01]$ GB structures when overlaid on the high-resolution transmission electron microscopy (HRTEM) images of the CeO_2 $\Sigma 3$ (111)/[$\bar{1}01$] GB that was reported by Feng et. al. [68] reveals an overlap of the Ce sub-lattice atoms along the {111} direction. See SI Figure 2. This suggests that the computationally considered structure has a qualitative match with the experimentally measured structure. For the $\Sigma 3$ (121)/[101] GB, a closely related system YSZ, atomic resolution structural information is also available. [69] A similar superposition of the computed $\text{CeO}_2 \Sigma 3 (121)/[\bar{1}01] \text{ GB}$ structure was made with the HRTEM image of YSZ $\Sigma 3$ (121)/[$\bar{1}01$] GB from Shibatta et. al. [69] and an overlap of the cation sub-lattice was evident along the {100} direction. See SI Figure 3. The undoped $\Sigma 3$ (111)/ $[\bar{1}01]$ GB cell has optimized lattice vectors [7.72, 7.72, 38.75] Å with 144 atoms and was converged with a 3x3x1 gamma-centered k-point grid. The undoped $\Sigma 3$ (121)/[$\bar{1}01$] GB cell has optimized lattice vectors [9.53, 7.74, 54.84] Å with 288 atoms and was converged with a 2x3x1 gamma-center k-point grid. A Gaussian smearing with a sigma value of 0.05 eV was employed.

During the initial construction of each GB supercell structure, the inter-GB spacing between respective grains (the z-axis separation) was set to maintain the same cation-anion bond distance across the interfaces as the grain interior. This was motivated by several studies suggesting that ceramic oxides relax to retain a bond length between ions that is similar to the grain interiors. [70, 71] To minimize the GB interactions between periodic images, the undoped GB cells were constructed from grains having a \mathbf{c} lattice vector two times the periodic repeat distance of the oriented cell, such that $\mathbf{c} = 2\mathbf{a}_{hkl}$, where hkl are the crystal directions associated with the (111) and (121) interfacial planes. These GB supercells are used for assessing the energy and electronic properties of the undoped and doped GBs. Note that the GB energy difference between the GB supercells constructed using grains with $\mathbf{c} = \mathbf{a}_{hkl}$ and $\mathbf{c} = 2\mathbf{a}_{hkl}$ was only 8 meV/Å² and 2 meV/Å² for the $\Sigma 3$ (111)/[$\bar{1}01$] and $\Sigma 3$ (121)/[$\bar{1}01$] GB, respectively.

We ensured that the strain fields due to the AEM solutes decayed within the supercell as discussed in the following section. When doped with an AEM solute, an oxygen vacancy was introduced in the cell to maintain charge neutrality. Pseudopotentials for each AEM solute were chosen such that the total energy was a minimum, and to ensure convergence of the simulations. The O and Ce atoms have been described by $2s^22p^4$ and $5s^25p^66s^25d^14f^1$ valence electrons, respectively. The valence electrons for Be and Mg were described by $2s^2$ and $3s^2$ while Ca, Sr, and Ba used $3s^23p^64s^2$, $4s^24p^65s^2$, $5s^25p^66s^2$ valence electrons, respectively. All structures considered in this study were subject to full structure optimization.

3. Results and discussion

3.1. Grain Boundary Structure and Character

Grain boundary notations represent its 5 macroscopic degrees of freedom, i.e., the four degrees specifying two directions and one specifying the angle. [72] Besides these macroscopic specifications, atomic-level parameters like the number of coordination-deficient cation sites, the average cation-anion bond distance, and the GB induced lattice expansion can further elucidate the GBs structure-property relationship. A coordination-deficient cation site is a site which has fewer bonds than that of the host cation in the defect-free lattice. Thus for ceria-based compounds, a coordination-deficient cation site will have less than 8 nearest neighbor oxygen atoms. GB expansion, $\gamma_{\rm GB}$ in Å, is defined as the difference in the z-axis length between the relaxed GB supercell and the corresponding relaxed GB-free supercell divided by two. Hence, $\gamma_{\rm GB}$ is a measure of the expansion of the pristine ceria's lattice vector that is perpendicular to the GB plane.

Table 1 lists the aforementioned atomic-scale parameters and the misorientation angles of the GBs. The $\Sigma 3$ (111)/[$\bar{1}01$] and $\Sigma 3$ (121)/[$\bar{1}01$] are both high-angle coincident site lattice boundaries [36] with misorientation angles of 35.26° and 54.74°, respectively. Interestingly, the equidistant (near cubic) polyhedral arrangement of the O ions around the Ce ions tend to remain intact at/near the GB core as can be seen in Figure 1. This can be attributed to the large ionicity of the Ce-O bonds. In order to retain the polyhedral arrangement of the host lattice the $\gamma_{\rm GB}$ is significant, 0.315 Å for $\Sigma 3$ (111)/[$\bar{1}01$] and 0.471 Å $\Sigma 3$ (121)/[$\bar{1}01$] GB, in agreement with experimentally measured values in similar systems. [70] We emphasize here that in stoichiometric ceria, the coordination-deficient vacancy sites are structural in origin. The charge neutrality of the compound is maintained for all simulations thus no other point defects were considered to be present at the GB.

The averaged Ce-O bond distance, $\bar{r}_{\rm Ce-O}^{~GB}$, in the $\Sigma 3~(111)/[\bar{1}01]$ and $\Sigma 3~(121)/[\bar{1}01]$ GB models are 2.379 Å and 2.385 Å, respectively. These average

Interface-Plane	θ (°)	sites	$\bar{r}_{\mathrm{Ce-O}}^{~GB}$ (Å)	$\gamma_{\rm GB} ({\rm \AA})$	$\Delta E_{ m GB}~({ m eV/\AA^2})$
$\Sigma 3~(111)/[ar{1}01]$	35.26	4	2.379	0.315	0.058 (0.93)
$\Sigma 3~(121)/[ar{1}01]$	54.74	4	2.385	0.471	0.093 (1.48)
YSZ $\Sigma 3 (111)/[\bar{1}01] [70]$	35.26	_	_	_	0.031 (0.49)
YSZ $\Sigma 3 (121)/[\bar{1}01] [70]$	54.74	_	_	_	0.037 (0.60)
poly. CeO ₂ [73]	_	_	_	_	0.105 (1.687)

Table 1: The interface-plane notation, the misorientation angle, θ in $^{\circ}$, the total number of coordination deficient cation sites per GB, the average Ce-O bond distance for each GB structure, $\bar{r}_{\text{Ce-O}}^{\ GB}$ in Å, the z-axis expansion of the GB supercell, γ_{GB} in Å and the GB energy, ΔE_{GB} in eV/Å² are listed for the two GBs studied in this work. ΔE_{GB} values listed in parenthesis are in J/m².

bond distances in the GBs are practically equal to the bond distances in bulk ceria, $r_{\rm Ce-O}^{CeO_2}=2.380$ Å. The excellent agreement between $\bar{r}_{\rm Ce-O}^{GB}$ and $r_{\rm Ce-O}^{CeO_2}$, however, does not imply that there are no distortions in the lattice upon incorporation of the GB. On the contrary, as shown in Figure 1c and e, up to $\pm 9\%$ bond deviation, $\Delta r_{\rm Ce-O}^{GB}=\frac{r_{\rm Ce-O}^{GB}-r_{\rm Ce-O}^{CeO_2}}{r_{\rm Ce-O}^{CeO_2}}\times 100$, where $r_{\rm Ce-O}^{GB}$ is the length of bonds in the GB structure, is observed. Both tensile and compressive strains are present in each GB lattice. The lattice distortions are predominant near the GB and diminish rapidly away from the GB.

3.2. Thermodynamic Descriptors of GBs and Solute Doped GBs

In order to compare the stability of ceria in the presence of GBs and dopants we compute the GB energy, $\Delta E_{\rm GB}$,

$$\Delta E_{\rm GB} = \frac{E_{\rm GB} - n_{\rm CeO_2} E_{\rm CeO_2} - n_{\rm MO} E_{\rm MO}}{2A} \tag{1}$$

where $E_{\rm GB}$ is the total energy of the GB supercell with solute M, E_{χ} is the energy of one formula unit of bulk χ where $\chi = {\rm CeO_2}$ or MO (see SI Table 1), n_{χ} is the number of formula units of χ in the GB supercell, and A is the area of the xy-plane i.e. the GB containing plane. $\Delta E_{\rm GB}$ represents the area normalized excess energy of ceria due to the creation of the GB interface.

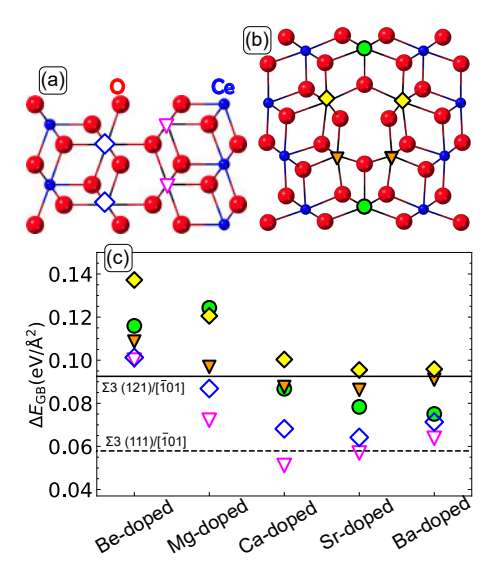


Figure 2: The a) $\Sigma 3$ (111)/[$\bar{1}01$] and b) $\Sigma 3$ (121)/[$\bar{1}01$] GB structures with all distinct solute sites indicated by a unique marker-color combination. All ions represented with a marker indicate a core GB cation site which was considered as potential substitutional site. c) $\Delta E_{\rm GB}$ for the $\Sigma 3$ (111)/[$\bar{1}01$] (open/dashed markers) and $\Sigma 3$ (121)/[$\bar{1}01$] (filled/solid markers) GBs. Each marker corresponds to the $\Delta E_{\rm GB}$ for each respective solute site depicted in the GB structure models.

As listed in Table 1, the $\Delta E_{\rm GB}$ of undoped $\Sigma 3$ (111)/[$\bar{1}01$] GB is approximately half the value of the $\Sigma 3$ (121)/[$\bar{1}01$] GB. This is not surprising since the $\Sigma 3$ (111)/[$\bar{1}01$] GB has a high atomic coherency across the interface, see Figure 1b and SI Figure 1a. The continuity of the anion and cation sublattices is clearly preserved in the $\Sigma 3$ (111)/[$\bar{1}01$] GB but the $\Sigma 3$ (121)/[$\bar{1}01$] GB has a disruption in the cation sublattice, see Figure 1d and SI Figure 1b. Other ceramic oxides such as YSZ, display similar dependence of the $\Delta E_{\rm GB}$ on the coherency of atoms at the interface. [71, 69, 70]

While experimental and theoretical reports of GB energies in these systems are scarce, available literature confirms that our GB energies are similar both in value as well as energetic trends. [70, 74, 73] One study using a multiphase equilibration technique [73] determined the GB energy for polycrystalline ${\rm CeO_2}$ to be 1.687 J/m² at 0 K. This value is reasonably close to our computed value.

ues that represent GBs possessing lower energies than one would expect in a polycrystalline ceramic.

YSZ, a closely related fluorite structured ceramic, has available experimental GB energies. [70] In this study the $\{111\}$ GB was found to possess lower GB energy ($\sim 0.49 \text{ J/m}^2$) while the $\{121\}$ GB was found to have a higher GB energy (0.6 J/m^2) . For our computed GB energies in CeO₂, the values for the undoped GBs follow the same energetic trend with the $\{111\}$ GB having the lowest GB energy and the $\{121\}$ GB having higher GB energy. Many theoretical calculations do not report GB energy values. For those studies that reference GB energies [74] typically refer to the study conducted by ref [68] implying GB energy values are around 1 J/m^2 .

Figure 2a and 2b mark the substitutional sites at the $\Sigma 3$ (111)/[$\bar{1}01$] and $\Sigma 3$ $(121)/[\bar{1}01]$ GB of ceria, respectively, where we place the Be, Mg, Ca, Sr, and Ba solutes to assess their impact on the stability, structure and electronic properties of the lattice. Note that higher concentration of dopants in ceria-based electrolytes at or near GBs [75, 76, 36] have been reported both experimentally [2, 3, 5, 6, 7, 77, 27, 78, 10] and theoretically [32, 30, 31, 79] to have higher local concentrations of solutes than usually found in the bulk. Local GB solute concentrations between 20%-40% have been verified by both atom-probe tomography [35] and atomic resolution transmission electron microscopy, [7, 5, 10] even when nominal solute concentrations are dilute (0.2%) [35]. By definition, for a cation site to be considered part of the GB core, the site must lie along/on either side of the GB mirror plane (see SI Figure 1). The $\Sigma 3$ (111)/[101] GB has two distinct sites, a coordination-deficient site marked by magenta triangles and a fully-coordinated site marked by blue diamonds. The $\Sigma 3$ (121)/[$\bar{1}01$] GB has three distinct sites, the coordination-deficient site marked by orange triangles and fully-coordinated sites marked by yellow diamonds and green circles. While the sites marked by green circles are fully-coordinated, they favor an asymmetric arrangement of the O-atoms around the site unlike the symmetric cubic arrangement in ceria.

A local GB solute concentration of 25% can be achieved for the $\Sigma 3 (111)/[\bar{1}01]$

and the $\Sigma 3$ (121)/[$\bar{1}01$] GBs by sequentially considering one core GB site (indicated by the markers in Figure 2a and 2b) within one region of the GB core for doping. A region within the GB core is assumed to have a 2 Å width perpendicular to the GB plane which originates at the cation mirror plane and extends towards the bulk. A total of 25 configurations of solutes were thus studied in this work. The large number of atoms in the simulation cell and the rapidly increasing number of configurations prohibit a comprehensive study of other solute concentrations.

Figure 2c shows that the $\Delta E_{\rm GB}$ is greater for the $\Sigma 3$ (121)/[$\bar{1}01$] GB than the $\Sigma 3$ (111)/[$\bar{1}01$] GB. Furthermore, for each substitutional site, $\Delta E_{\rm GB}$ has a parabolic dependence on the solute cation's ionic radius. The site-dependence of the $\Delta E_{\rm GB}$ of the $\Sigma 3$ (111)/[$\bar{1}01$] GB is low in comparison to that of the $\Sigma 3$ (121)/[$\bar{1}01$] GB. This can be understood by examining the net bond strain at the dopant sites of the GBs shown in Figure 1c and 1e. In the $\Sigma 3$ (121)/[$\bar{1}01$] GB, the three distinct solute sites have markedly different net bond strain illustrated by the variation in color in Figure 1c, 1e, and SI Figure 13-14. The net tensile to compressive bond strain ratio is highest in the green-site, intermediate in the yellow site and lowest in the orange site. In comparison, the blue and magenta sites in the $\Sigma 3$ (111)/[$\bar{1}01$] GB have similar net bond strains as the $\Sigma 3$ (121)/[$\bar{1}01$] GB, but much smaller overall net bond strains shown in Figure 1c.

For both the GBs, the coordination-deficient cation sites (magenta and orange triangles) are among the lowest energy sites. For the $\Sigma 3$ (121)/[$\bar{1}01$] GB, the fully-coordinated sites marked by the green circle also have low $\Delta E_{\rm GB}$, especially for the heavier solute cations. These three low $\Delta E_{\rm GB}$ sites are also the most strained sites in the GBs. The blue sites in the $\Sigma 3$ (111)/[$\bar{1}01$] GB and the yellow sites in the $\Sigma 3$ (121)/[$\bar{1}01$] GB have largest energies displaying a barrier for doping and preference for the Ce-atoms to remain in a site that has coordination and bond-length similar to that of the grain interior. Similar trends in four symmetric tilt GBs have been observed for YSZ. [71, 70]

It is noteworthy that the addition of Be and Mg make the GBs consistently more unstable across all sites. Apart from the large mismatch in the ionic radii of Ce $(R_i = 0.97 \text{ Å})$ with that of Be $(R_i = 0.27 \text{ Å})$ and Mg $(R_i = 0.57 \text{ Å})$ [80], the nature of bonding in the native oxides of Mg and Be also dictates the stability of the GB. Unlike the octahedral coordination predominant in Ca $(R_i = 1.12 \text{ Å})$, Sr $(R_i = 1.42 \text{ Å})$ and Ba $(R_i = 1.26 \text{ Å})$ oxides, Be and Mg oxides display a tetrahedral bonding (see SI Table 1). The Be and Mg dopants relax into interstitial sites to attain this 4-fold coordination where possible, for example, in some of the coordination-deficient sites. The relaxed structure of all solute configurations are presented in the SI Figure 13-14. Since the Ca dopants have the lowest mismatch in the ionic radii with the host Ce atoms and also more closely match the cubic coordination of the host cation, these solutes render the GB most stable in comparison to the other solutes.

Overall, the $\Delta E_{\rm GB}$ critical point appears to be modulated by three primary factors: (a) the local atomic environment of the solute site, (b) the solute size and (c) the coordination of the solute in its native oxide. The relative difference in $\Delta E_{\rm GB}$ between the GBs may be due to the GB packing density. Furthermore, it is evident that the $\Delta E_{\rm GB}$ can be more easily modulated by varying the solute type and is much less weakly modulated by the substitutional site. Additionally, GB doping strategies attempting to smooth out the potential energy landscape across GBs should focus on Ca or Sr solutes because the lowest GB energies, out of the five solute sites explored, is achieved for the Ca and Sr solutes.

3.3. Electronic Structure of AEM Doped Ceria

Aliovalent solutes are often used to increase the number of charge carriers in ceramic oxides. [81] Although, they can also introduce localized defect states and/or bands above the band gap activating electronic conduction mechanisms such as polaron hopping, [82, 83] which can be detrimental to the ionic conductivities. In this section, we show that the AEM solutes can deactivate these potentially detrimental electronic conduction mechanisms. In this context, we find that AEM solutes do not introduce any defect states above the valence band or in the band gap as discussed below.

Figure 3a and b show the element-projected density of states (DOS) for the

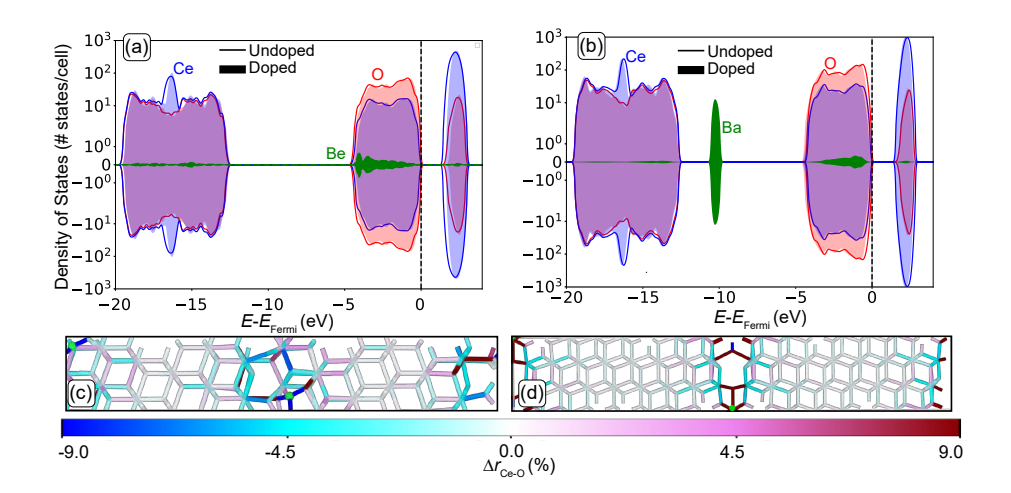


Figure 3: The element-projected DOS for the a) undoped (solid lines) and Be-doped (shaded regions) for the $\Sigma 3$ (111)/[$\bar{1}01$] GBs, and b) undoped (solid lines) and Ba-doped (shaded regions) for the $\Sigma 3$ (121)/[$\bar{1}01$] GBs. The $\Delta r_{\rm Ce-O}^{~GB}$ of the Be-doped $\Sigma 3$ (111)/[$\bar{1}01$] GB is shown in (c) and that of the Ba-doped $\Sigma 3$ (121)/[$\bar{1}01$] GB is shown in (d). Blue indicates compressed bonds while red indicates tensile bonds. The DOS is shifted such that the top of the valence band is at 0 eV.

supercells with the $\Sigma 3$ (111)/[$\bar{1}01$] and $\Sigma 3$ (121)/[$\bar{1}01$] GB, respectively. The solid lines show the DOS for the undoped GB and the shaded regions mark the DOS for the solute-doped GB. From the DOS, it is clear that the incorporation of Be and Ba solutes at the GB core does not result in defect states above the band gap or within it. Similarly, we find that none of the solutes impart defect states, see SI Figure 8-12.

In the undoped GB, the states at the conduction band maxima (CBM) are dominated by Ce-4f and O-2p states with smaller contributions from Ce-4d and 5p states. See SI Figure 9-12 for orbital-projected density of states. The states at the valence band minima (VBm) are mostly O-2p states.

Negligible changes occur in the states present at the VBm and CBM upon doping. For all but the Be-doped GBs, d, p and s states of the solute atom are present at the CBM, resulting in distorted cubic bonding of the solute-O bonds at the GB, see Figure 3d and SI Figure 9-12. For Be-doped GBs, only p and s states of the Be are present at the CBM, indicating a strong propensity of Be

to form tetrahedral Be-O bonds as shown in Figure 3c.

Figure 4 shows that, relative to bulk ceria, the presence of the GBs and solutes have a significant impact on the band gap. The presence of the planar defect, the GB, results in a decrease in the $E_{\rm gap}$ with calculated $E_{\rm gap}$ values for the $\Sigma 3$ (111)/[$\bar{1}01$] GB and $\Sigma 3$ (121)/[$\bar{1}01$] GB of 1.61 eV and 1.72 eV, respectively. The incorporation of solutes can modulate the band gap further, by up to 0.3 eV relative to the undoped GB. A close inspection of the occupied states in the DOS of AEM doped GBs reveals that the states well below the Fermi level alter the Ce-O bonded states in a manner that the $E_{\rm gap}$ decreases with respect to the bulk.

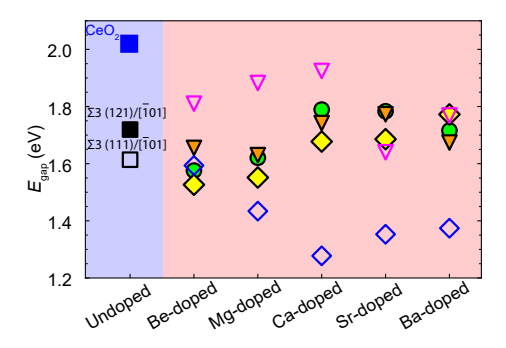


Figure 4: a) The $E_{\rm gap}$ for each solute-GB configuration. The undoped GBs are represented with black squares and the bulk ceria by blue square. The $\Sigma 3$ (121)/[$\bar{1}01$] GB shows minor site and solute dependence while the $\Sigma 3$ (111)/[$\bar{1}01$] GB shows both site and solute dependence.

Strain has been shown to strongly alter the band gap of bulk ceria [84, 85]. SI Figure 7 shows the strain-dependent change in band gap of bulk ceria. The band gap is found to be linearly dependent on the uniform hydrostatic strain of the bulk ceria lattice. A band gap difference of 0.4 eV is observed for compressive strain of 4% and -0.4 eV band gap difference for a tensile strain of 4% with respect to the unstrained lattice. A compressive strain results in a band gap increase and a tensile strain results in a band gap reduction compared to the unstrained lattice. SI Figure 7 also shows that sub-0.05 eV band gap differences can be resolved in our simulations.

We find a solute and site dependent band gap variation of about 0.7 eV

for the $\Sigma 3$ (111)/[$\bar{1}01$] GB and about 0.2 eV for the $\Sigma 3$ (121)/[$\bar{1}01$] GB. The various solutes in the different sites lead to change in the lattice parameters of the supercell resulting in volumetric strains of the lattice that are between -1% to 1.5%, see SI Figure 6. The lattice strains in the doped GBs, however, are not large enough to result in the observed solute and site dependent band gap variations. For instance in the case of Ca-doped $\Sigma 3$ (111)/ $[\bar{1}01]$ GB, a difference of about 0.7 eV is observed for the magenta triangle and blue diamond sites of Ca-doped $\Sigma 3$ (111)/[$\bar{1}01$] GB. As noted in the SI Figure 6(a), the volumetric change in the lattice of the Ca-doped $\Sigma 3$ (111)/ $[\bar{1}01]$ CeO₂ GBs with respect to the unstrained GBs is \sim -0.2% for the blue diamond site and \sim 0.3% for the magenta triangle site. Similar to bulk CeO₂, we find that the magenta triangle site has a band gap increase and the blue diamond site has a band gap decrease due to the compressive and tensile strains, respectively. However, based on the strain-dependent band gap change in the bulk ceria, it is evident that such a small lattice strain cannot be the cause of a ${\sim}0.7$ eV difference between the band gap for the magenta triangle and the blue diamond sites. In order to make a direct comparison with undoped $\Sigma 3$ (111)/[$\bar{1}01$] GB, we applied hydrostatic strain to undoped $\Sigma 3$ (111)/ $[\bar{1}01]$ GB and found a similar level of change in the band gap as the bulk ceria lattice, -0.26 eV for 2% strain and 0.26 eV for -2% strain.

In opposition to the lattice strains, the local strains around the solute site in these two cases are markedly different and an order of magnitude larger. SI Figure 13 shows that the local strain around the magenta triangle site is predominantly compressive, about -5%, and predominantly tensile around the blue diamond site, about 5%-9%. While we cannot prove with certainty that the local strains are the cause of the large site-dependent band gap variation, based on elimination of the lattice-strain and inadequate numerical accuracy as underlying causes, it becomes a possible explanation for the solute-site dependent band gap variation.

For the $\Sigma 3$ (121)/[$\bar{1}01$] GBs, the band gap changes are well correlated with the average Ce-O bond distances, see SI Figure 4, and fluctuate around the

undoped $\Sigma 3$ (121)/[$\bar{1}01$] GB band gap. However, for the doped $\Sigma 3$ (111)/[$\bar{1}01$] GB the band gaps appear to be modulated by three main factors: bond strain, local atomic environment of the GB core, and the ionic radii of the solute atom. The coordination-deficient sites (magenta triangle) in the $\Sigma 3$ (111)/[$\bar{1}01$] GB have less strain than the fully-coordinated sites (blue diamond) resulting in a linear increase in the band gap, see SI Figure 13. This trend continues until Sr and Ba where the band gap values decrease, an effect which most likely originates from the increased bond strain which extends well into the bulk and can be seen in SI Figure 13. The fully-coordinated sites (blue diamond symbols) are unable to relax since they are sterically hindered by the surrounding anions. The increased strain for these sites which increase the hybridization between the Ce 4f - O 2p - M nd, np and ns states, where M = Ca, Sr, and Ba and n is the principle quantum number, decreasing the band gap which can be seen in SI Figure 9. For both the GBs, the Ba-doped ceria maintains a similar band gap compared with the undoped GB samples for all sites considered.

In all, the band gap in ceria is considerably affected by the presence of both planar and solute defects. This can result in heterogeneous electronic properties in experimentally synthesized nanocrystalline ceria. The changes in the band gap due to both solutes and the presence of GBs are correlated with the local atomic structure of the GB, average Ce-O bond distance, and the bond strain. Furthermore, the sensitivity of the electronic structure may be modulated by the GB packing density. For close packed GBs, sites that are sterically hindered may have increased hybridization, thereby decreasing the band gap; whereas unhindered sites show a linear increase in the band gap.

3.4. Possible Impact of High Dopant Concentrations on Oxide Grain Boundaries

Fundamental studies of grain boundaries in oxide ceramics with the presence of dopants increases the phase-space that needs to be considered, thus, significantly increasing the computational cost and time. The recent advances in computing power makes these much-needed foundational investigations with DFT feasible. Our ab-initio study on ceria provides critical guidance to larger-

length- and time-scale simulations such as molecular dynamics and Monte Carlo simulations. [86, 33, 79] Additionally, this lays the foundation for future work exploring relevant GB effects such as space-charge layers. [87]

Previously, researchers [68] have emphasized the importance of investigations that focus on the atomic- and electronic-level properties of different GBs due to their diversity. Currently, the critical factors influencing microscopic properties (such as local bonding, strain and space charge layers) are not understood from an atomic scale perspective. There are many open questions regarding the role and impact that the atomic structure, solute size, local bond strain and composition, as well as the electronic properties play in GB structure-property relationships for this important class of ceramics. Even basic correlations regarding the site-dependent stability of solutes located at GBs was previously unexplored for these systems, often relying on interatomic potentials fit to bulk properties to gain insight into the GB problem. [86, 33, 79]

In ceria, we have found that the GBs possessing less structural coherency have higher GB energies, yet, these energies stabilize when doped with solutes that are larger than the host solute. In general, this is consistent with the principle that coherent interfaces are lower in energy and stable. Solutes that are smaller in ionic radii than the host solute result in a less coherent GB structure and increase the GB energy. Less structural coherency has been previously associated with higher GB energies in fluorite oxides, [71, 69, 70] as well as in similar systems such as YSZ. This trend indicates that ionic materials may exhibit a strong energetic dependence on the structural coherency across the GB. Strategies that aim to decrease the GB energy by doping should focus on solutes larger than the host solute whilst avoiding smaller solutes that render the GB unstable. A large mismatch between the host and solute ions increases the likeliness of solute segregation and oxygen vacancy binding [79] to the GB. Additionally, co-doping with different solutes may be a feasible strategy to optimize both the bulk and GB properties.

The location of the solute within the GB core results in appreciable modulations in the GB energy. However, there is a clear dependence of the GB energy on the solute size indicating that the type of solute may play a more important role in minimizing the GB energy than the location of the solute. Additionally, the choice of solute, unlike the location of the solute, is accessible via experimental methods. Therefore, it is critically important to carefully select solutes to optimize the GB properties. Future computational work should be directed towards three main areas: 1) identifying solutes that decrease the GB energy, 2) identifying solutes that possess a high GB segregation energy, and 3) possess a low oxygen vacancy binding for ionic conductors.

For applications that depend upon high ionic conductivity, changing the electronic properties via doping is undesirable. Thus, understanding how band gaps are modulated due to the presence of solutes, interfacial strain, and GB character is essential to predict suitable solutes that do not significantly perturb the electronic structure near the band gap. Our study demonstrates that the DOS profile around $E_{\rm gap}$ remains unchanged and that the $E_{\rm gap}$ value is perturbed due to the presence of the solutes and GB.

4. Conclusions

In conclusion, we use DFT with the GGA+U functional to examine the structure, energetic stability and electronic properties of undoped and alkaliearth metal doped GBs in ceria. We studied two high-angle grain boundaries, the $\Sigma 3$ (111)/[$\bar{1}01$] and the $\Sigma 3$ (121)/[$\bar{1}01$] GB and find that the $\Sigma 3$ (111)/[$\bar{1}01$] GB is energetically more stable than the $\Sigma 3$ (121)/[$\bar{1}01$] GB due to its larger atomic coherency at the GB interface.

To-date, there are no other theoretical studies that exhaustively assess this atomic-scale role of dopants in grain boundaries of ceria, or similar oxide-based systems. Foundational studies such as this are imperative to address questions about the effect of dopants in these well studied, technological relevant materials. Our study addresses this need providing a systematic assessment of the local atomic structure, GB geometry, and solutes to determine how these factors modulate GB thermodynamics as well as the electronic properties of the GB.

Considering all the substitutional sites in the GB core, we find that when the GBs are doped with $\sim 20\%$ AEM solutes, the GB energies of ceria will depend strongly on the substitutional site's coordination numbers and its local atomic structure. We identify the lowest energy substitutional sites for each AEM dopant and find that Ca, Sr and Ba solutes stabilize the GBs but Be and Mg solutes render the GBs unstable. The enhancements in the GB stability upon addition of Ca, Sr and Ba can be attributed to similarity in the ionic radii of the solutes and Ce as well as the closely matching coordination of the solute in its native oxide and the ceria lattice. The electronic density of states of doped GBs reveals that no defect states are present in or above the band gap of the AEM doped ceria, which is highly conducive to maintaining low electronic mobility in these ionic conductors. The electronic properties, unlike the energetic stability, exhibit complex inter-dependence on the structure and chemistry of the host and the solutes. The presence of dopants can modulate the band gap of ceria up to 0.3 eV in comparison to the undoped ceria with GBs.

Our results reinforce the claims of Bokov et. al. [76] that solutes can smooth out the energy landscape thereby reducing the GB energy. This smooth potential energy landscape (lower GB energy) could result in an increase in ionic conductivity across GBs and thus a critical factor to consider in optimizing these functional ceramics. Additionally, our results indicate that solutes slightly larger than the host cation stabilize the GB more strongly. Correlations believed to apply in metallic systems such as the GB energy being related to the excess volume at the interface [88] do not hold for systems that are dominated by ionic bonding, as evident when comparing Figure 2c with SI Figure 6 where there is no correlation between the GB expansion (in any direction) with GB energy.

In the future, advances in computational methods and computing power can enable a comprehensive first-principles based study of more GB structures, solute concentrations as well as the coordinated transport of oxygen-vacancies and ions. Our work serves as a guide to these future studies, making an impact on the design of more efficient oxide based ionic conductors.

5. Acknowledgements

The authors thank start-up funds from Arizona State University and the National Science Foundation grant number DMR-1308085, DMR-1840841, and DMR-1906030. This work used the Extreme Science and Engineering Discovery Environment (XSEDE), which was supported by National Science Foundation grant number TG-DMR150006. The authors acknowledge Research Computing at Arizona State University for providing HPC resources that have contributed to the research results reported within this paper.

6. Supporting Information

Supporting information provides a detailed analysis of the GB structure, symmetry, and associated cation site symmetries for each GB to elucidate the connection between local GB structure and strain. The symmetry, structural, and energetic properties of all stable bulk oxide compounds with stoichiometry MO are compiled. The average Ce-O bond distance, z-axis GB expansion, and percent change in the volume of the solute ion doped GB structures is also shown. All element and orbital projected DOS and bond strain maps are provided for each solute-GB structure. Finally, the results from the hydrostatic strain induced band gap changes are provided in support of our electronic structure analysis section.

References

- A. P. Sutton, R. W. Balluffi, Interfaces in Crystalline Materials, Clarendon Press, 1995, pp. 1–798 (1995).
- [2] N. D. Browning, R. F. Klie, Y. Y. Lei (Eds.), Mixed Ionic Electronic Conducting Perovskites for Advanced Energy Systems, 2004, pp. 2015–2025 (2004).

- [3] W. Lee, H. J. Jung, M. H. Lee, Y. B. Kim, J. S. Park, R. Sinclair, F. B. Prinz, Oxygen surface exchange at grain boundaries of oxide ion conductors, Advanced Functional Materials 22 (2012) 965–971 (2012).
- [4] F. Ye, C. Y. Yin, D. R. Ou, T. Mori, Relationship between lattice mismatch and ionic conduction of grain boundary in YSZ, Progress in Natural Science-Materials International 24 (2014) 83–86 (2014).
- [5] W. J. Bowman, J. Zhu, R. Sharma, P. A. Crozier, Electrical conductivity and grain boundary composition of Gd-doped and Gd/Pr co-doped ceria, Solid State Ionics 272 (2015) 9–17 (2015).
- [6] Y. Lin, S. Fang, D. Su, K. S. Brinkman, F. Chen, Enhancing grain boundary ionic conductivity in mixed ionic-electronic conductors, Nature Communications 6 (2015).
- [7] W. J. Bowman, M. N. Kelly, G. S. Rohrer, C. A. Hernandez, P. A. Crozier, Enhanced ionic conductivity in electroceramics by nanoscale enrichment of grain boundaries with high solute concentration, Nanoscale 9 (2017) 17293–17302 (2017).
- [8] B. Feng, N. R. Lugg, A. Kumamoto, Y. Ikuhara, N. Shibata, Direct observation of oxygen vacancy distribution across yttria-stabilized zirconia grain boundaries, ACS Nano 11 (2017) 11376–11382 (2017).
- [9] N. Nafsin, T. J. A. Aguiar, A. M. Aoki, K. v. B. Thron, R. H. R. Castro, Thermodynamics versus kinetics of grain growth control in nanocrystalline zirconia, Acta Materialia (2017) 224–234 (2017).
- [10] W. J. Bowman, A. Darbal, P. A. Crozier, Linking macroscopic and nanoscopic ionic conductivity: Towards a new semi-empirical framework for characterizing grain boundary conductivity in polycrystalline ceramics, ACS Applied Materials & Interfaces 12 (2020) 507–517 (2020).
- [11] A. Trovarelli, Catalysis by ceria and related materials, Imperial College Press, London, 2002 (2002).

- [12] J. Paier, C. Penschke, J. Sauer, Oxygen defects and surface chemistry of ceria: Quantum chemical studies compared to experiment, Chemical Reviews 113 (2013) 3949–3985 (2013).
- [13] S. C. Singhal, K. E. Kendall, High Temperature Solid Oxide Fuel Cells, Elsevier, New York, 2003 (2003).
- [14] E. D. Wachsman, K. T. Lee, Lowering the temperature of solid oxide fuel cells, Science 334 (2011) 935–939 (2011).
- [15] E. D. Wachsman, C. A. Marlowe, K. T. Lee, Role of solid oxide fuel cells in a balanced energy strategy, Energy & Environmental Science 5 (2012) 5498–5509 (2012).
- [16] J. Sunarso, S. Baumann, J. M. Serra, W. A. Meulenberg, S. Liu, Y. S. Lind, J. C. D. da Costa, Mixed ionic-electronic conducting (MIEC) ceramicbased membranes for oxygen separation, Journal of Membrane Science 320 (2008) 13–41 (2008).
- [17] L. Zhang, N. Xu, X. Li, S. Wang, K. Huang, W. H. Harris, W. K. S. Chiu, High CO₂ permeation flux enabled by highly interconnected three-dimensional ionic channels in selective CO₂ separation membranes, Energy & Environmental Science 5 (2012) 8310–8317 (2012).
- [18] S. M. Haile, D. L. West, J. Campbell, The role of microstructure and processing on the proton conducting properties of gadolinium-doped barium cerate, Journal of Materials Research 13 (1998) 1576–1595 (1998).
- [19] S. Schweiger, R. Pfenninger, W. J. Bowman, U. Aschauer, J. L. M. Rupp, Designing strained interface heterostructures for memristive devices, Advanced Materials 29 (2017) 11 (2017).
- [20] D. R. Franceschetti, Local thermodynamic formalism for space-charge in ionic-crystals, Solid State Ionics 2 (1981) 39–42 (1981).

- [21] J. Maier, Ionic-conduction in space charge regions, Progress in Solid State Chemistry 23 (1995) 171–263 (1995).
- [22] X. Guo, J. Maier, Grain boundary blocking effect in zirconia: A schottky barrier analysis, Journal of the Electrochemical Society 148 (2001) E121– E126 (2001).
- [23] J. S. Lee, D. Y. Kim, Space-charge concepts on grain boundary impedance of a high-purity yttria-stabilized tetragonal zirconia polycrystal, Journal of Materials Research 16 (2001) 2739–2751 (2001).
- [24] X. Guo, W. Sigle, J. Maier, Blocking grain boundaries in yttria-doped and undoped ceria ceramics of high purity, Journal of the American Ceramic Society 86 (2003) 77–87 (2003).
- [25] H. L. Tuller, Ionic Conduction and Applications, Springer Verlag, New York, 2006, pp. 213–228 (2006).
- [26] H. L. Tuller, S. R. Bishop, Tailoring material properties through defect engineering, Chemistry Letters 39 (2010) 1226–1231 (2010).
- [27] Y. Y. Lei, Y. Ito, N. D. Browning, T. J. Mazanec, Segregation effects at grain boundaries in fluorite-structured ceramics, Journal of the American Ceramic Society 85 (2002) 2359–2363 (2002).
- [28] M. Shirpour, B. Rahmati, W. Sigle, P. A. van Aken, R. Merkle, J. Maier, Dopant segregation and space charge effects in proton-conducting bazro₃ perovskites, Journal of Physical Chemistry C 116 (2012) 2453–2461 (2012).
- [29] J. An, J. S. Park, A. L. Koh, H. B. Lee, H. J. Jung, J. Schoonman, R. Sinclair, T. M. Gur, F. B. Prinz, Atomic scale verification of oxide-ion vacancy distribution near a single grain boundary in YSZ, Scientific Reports 3 (2013).
- [30] H. B. Lee, F. B. Prinz, W. Cai, Atomistic simulations of grain boundary segregation in nanocrystalline yttria-stabilized zirconia and gadolinia-

- doped ceria solid oxide electrolytes, Acta Materialia 61 (2013) 3872–3887 (2013).
- [31] D. R. Diercks, J. H. Tong, H. Y. Zhu, R. Kee, G. Baure, J. C. Nino, R. O'Hayre, B. P. Gorman, Three-dimensional quantification of composition and electrostatic potential at individual grain boundaries in doped ceria, Journal of Materials Chemistry A 4 (2016) 5167–5175 (2016).
- [32] D. S. Mebane, R. A. D. Souza, A generalised space-charge theory for extended defects in oxygen-ion conducting electrolytes: from dilute to concentrated solid solutions, Energy & Environmental Science 8 (2015) 2935–2940 (2015).
- [33] D. S. Aidhy, Y. W. Zhang, W. J. Weber, Impact of segregation energetics on oxygen conductivity at ionic grain boundaries, Journal of Materials Chemistry A 2 (2014) 1704–1709 (2014).
- [34] D. E. P. Vanpoucke, P. Bultinck, S. Cottenier, V. V. Speybroeckb, I. V. Driessche, Aliovalent doping of CeO₂: DFT study of oxidation state and vacancy effects, Journal of Materials Chemistry A 2 (2014) 13723 (2014). doi:10.1039/c4ta02449d.
- [35] X. Xu, Y. Liu, J. Wang, D. Isheim, V. Dravid, C. Phatak, S. Haile, Variability and origins of grain boundary electric potential detected by electron holography and atom-probe tomography, Nature Materials (2020). doi:https://doi.org/10.1038/s41563-020-0656-1.
- [36] W. J. Bowman, Correlating Nanoscale Grain Boundary Composition with Electrical Conductivity in Ceria, Arizona State University, 2016 (2016).
- [37] P. E. Blochl, Projector augmented-wave method, Physical Review B 50 (1994) 17953 (1994).
- [38] G. Kresse, D. Joubert, From ultrasoft pseudopotentials to the projector augmented-wave method, Physical Review B 59 (1999) 1758 (1999).

- [39] G. Kresse, J. Hafner, Ab initio molecular dynamics for liquid metals, Physical Review B 47 (1993) 558 (1993).
- [40] G. Kresse, J. Hafner, Ab initio molecular-dynamics simulation of the liquidmetal-amorphous-semiconductor transition in germanium, Physical Review B 49 (1994) 14251 (1994).
- [41] G. Kresse, J. Furthmüller, Efficiency of ab-initio total energy calculations for metals and semiconductors using a plane-wave basis set, Computional Materials Science 6 (1996) 15 (1996).
- [42] G. Kresse, J. Furthmüller, Efficient iterative schemes for ab initio totalenergy calculations using a plane-wave basis set, Physical Review B 54 (1996) 11169–11186 (1996). doi:10.1103/PhysRevB.54.11169. URL https://link.aps.org/doi/10.1103/PhysRevB.54.11169
- [43] J. P. Perdew, K. Burke, M. Ernzerhof, Generalized gradient approximation made simple, Physical Review Letters 77 (1996) 3865 (1996).
- [44] J. P. Perdew, K. Burke, M. Ernzerhof, Erratum generalized gradient approximation made simple, Physical Review Letters 78 (1997) 1396 (1997).
- [45] S. L. Dudarev, G. A. Botton, S. Y. Savrasov, C. J. Humphreys, A. P. Sutton, Electron-energy-loss spectra and the structural stability of nickel oxide: An LSDA+U study, Physical Review B 57 (1998) 1505–1509 (1998). doi:10.1103/PhysRevB.57.1505.
- [46] P. P. Dholabhai, J. B. Adams, P. Crozier, R. Sharma, Oxygen vacancy migration in ceria and Pr-doped ceria: A DFT+U study, Journal of Chemical Physics 132 (2010) 1–8 (2010).
- [47] J. Koettgen, M. Martin, The effect of jump attempt frequency on the ionic conductivity of doped ceria, Journal of Physical Chemistry C 123 (2019) 19437–19446 (2019).

- [48] J. Koettgen, M. Martin, Infinite dilution in doped ceria and high activation energies, Solid State Communications (2020) 113939 (2020).
- [49] P. P. Dholabhai, J. B. Adams, P. Crozier, R. Sharma, A density functional study of defect migration in gadolinium doped ceria, Physical Chemistry Chemical Physics 12 (2010) 7904 (2010).
- [50] H. Zhu, H. Yongchun, R. Hao, L. Dongyuan, L. Xin, Z. Lianming, C. Yuhua, G. Wenye, Theoretical investigation of h2 oxidation mechanisms over pristine and Sm-doped CeO₂ (111) surfaces, Applied Surface Science 511 (2020) 145388 (2020).
- [51] L. Gerward, J. S. Olsen, Powder diffraction analysis of cerium dioxide at high pressure, Powder Diffraction 8 (1993) 127–129 (1993). doi:10.1017/ S0885715600017966.
- [52] K. A. Gschneider, L. Eyring (Eds.), Handbook on the Physics and Chemistry of Rare Earths, Vol. 3, North-Holland, Amsterdam, 1979, Ch. 27, pp. 1–664 (1979).
- [53] A. Nakajima, A. Yoshihara, M. Ishigame, Defect-induced raman spectra in doped CeO₂, Physical Review B 50 (1994) 13297–13307 (1994). doi: 10.1103/PhysRevB.50.13297.
- [54] L. He, F. Liu, G. Hautier, M. J. T. Oliveira, M. A. L. Marques, F. D. Vila, J. J. Rehr, G.-M. Rignanese, A. Zhou, Accuracy of generalized gradient approximation functionals for density-functional perturbation theory calculations, Physical Review B 89 (6) (2014) 064305 (2014). doi: 10.1103/PhysRevB.89.064305.
- [55] T. Wu, T. Vegge, H. A. Hansen, Improved electrocatalytic water splitting reaction on CeO_2 (111) by strain engineering, ACS Catalysis 9 (2019) 4853–4861 (2019).

- [56] J. Perdew, Density functional theory and the band gap problem, Journal of Quantum Chemistry 28 (1985) 497–523 (1985). doi:https://doi.org/ 10.1002/qua.560280846.
- [57] J. Jie, M. Weng, S. Li, D. Chen, S. Li, W. Xiao, J. Zheng, F. Pan, L. Wang, A new materialgo database and its comparison with other high-throughput electronic structure databases for their predicted energy band gaps, Science China Technological Sciences 62 (2019) 1423–1430 (2019). doi:https://doi.org/10.1007/s11431-019-9514-5.
- [58] A. Dittmer, R. Izsák, F. Neese, D. Maganas, Accurate band gap predictions of semiconductors in the framework of the similarity transformed equation of motion coupled cluster theory, Inorganic Chemistry 58 9303–9315. doi: 10.1021/acs.inorgchem.9b00994.
- [59] E. Brothers, A. Izmaylov, J. Normand, V. Barone, G. Scuseria, Accurate solid-state band gaps via screened hybrid electronic structure calculations, The Journal of Chemical Physics 129 (2008).
- [60] S. A. Tolba, K. M. Gameel, B. A. Ali, H. A. Almossalami, N. K. Allam, Recent Progresses of Theory and Application, IntechOpen, 2018 (2018). doi:10.5772/intechopen.72020.
- [61] M. Chan, G. C, Efficient band gap predictions for solids, Physical Review Letters 19 (2010).
- [62] J. Heyd, J. Peralta, G. Scuseria, R. Martin, Energy band gaps and lattice parameters evaluated with the heyd-scuseria-ernzerhof screened hybrid functional, Journal of Chemical Physics 123 (2005).
- [63] W. Setyawan, R. Gaume, S. L. R. Feigelson, S. Curtarolo, High-throughput combinatorial database of electronic band structures for inorganic scintillator materials, ACS Combinatorial Science (2011).
- [64] G. Kresse, M. Marsman, J. Furthmuller, VASP Manual, Universitat Wien, Vienna (2018).

- [65] H. Hellman, An Introduction to Quantum Chemistry, Deuticke, Leipzig, 1937 (1937).
- [66] C. G. Broyden, A class of methods for solving nonlinear simultaneous equations, Mathematics of Computation 19 (1965) 577–593 (1965).
- [67] S. P. Ong, W. D. Richards, A. Jain, G. Hautier, M. Kocher, S. Cholia, D. Gunter, V. L. Chevrier, K. A. Persson, G. Ceder, Python Materials Genomics (pymatgen): A robust, open-source python library for materials analysis, Computational Materials Science 68 (2013) 314–319 (2013). doi: 10.1016/j.commatsci.2012.10.028.
- [68] B. Feng, H. Hojo, T. Mizoguchi, H. Ohta, S. D. Findlay, Y. Sato, N. Shibata, T. Yamamoto, Y. Ikuhara, Atomic structure of a $\sigma 3$ [110]/(111) grain boundary in CeO₂, Applied Physics Letters 100 (2012) 3–6 (2012). doi:10.1063/1.3682310.
- [69] N. Shibata, F. Oba, T. Yamamoto, T. Sakuma, Y. Ikuhara, Grain-boundary faceting at a $\Sigma=3$, [110]/{112} grain boundary in a cubic zirconia bicrystal, Philosophical Magazine 83 (2003) 2221–2246 (2003). doi:10.1080/0141861031000108231.
- [70] N. Shibata, F. Oba, T. Yamamoto, Y. Ikuhara, Structure, energy and solute segregation behaviour of [110] symmetric tilt grain boundaries in yttria-stabilized cubic zirconia, Philosophical Magazine 84 (2004) 2381– 2415 (2004).
- [71] N. Shibata, F. Oba, T. Yamamoto, Y. Ikuhara, T. Sakuma, Atomic structure and solute segregation of a $\Sigma=3$, [110]/{111} grain boundary in an yttria-stabilized cubic zirconia bicrystal, Philosophical Magazine Letters 82 (2002) 393–400 (2002). doi:10.1080/09500830210137407.
- [72] V. Randle, The Measure of Grain Boundary Geometry, Institute of Physics Publishing, 1993 (1993).

- [73] N. Zouvelou, X. Mantzouris, P. Nikolopoulos, Surface and grain-boundary energies as well as surface mass transport in polycrystalline CeO₂, Materials Science and Engineering: A 495 (2008) 54–59 (2008). doi:https://doi. org/10.1016/j.msea.2007.10.105.
- [74] F. Yuan, B. Liu, Y. Zhang, W. J. Weber, Segregation and Migration of the Oxygen Vacancies in the Σ 3 (111) Tilt Grain Boundaries of Ceria, Journal of Physical Chemistry C 120 (12) (2016) 6625–6632 (2016). doi: 10.1021/acs.jpcc.6b00325.
- [75] P. P. Dholabhai, J. A. Aguiar, L. Wu, T. G. Holesinger, T. Aoki, R. H. R. Castro, B. P. Uberuaga, Structure and segregation of dopant–defect complexes at grain boundaries in nanocrystalline doped ceria, Physical Chemistry Chemical Physics 17 (2015) 15375–15385 (2015).
- [76] A. Bokov, J. A. Aguiar, M. L. Gong, A. Nikonov, R. H. R. Castro, A Strategy to Mitigate Grain Boundary Blocking in Nanocrystalline Zirconia, Journal of Physical Chemistry C 122 (2018) 26344–26352 (2018). doi: 10.1021/acs.jpcc.8b08877.
- [77] H. J. Avila-Paredes, S. Kim, The effect of segregated transition metal ions on the grain boundary resistivity of gadolinium doped ceria: Alteration of the space charge potential, Solid State Ionics 177 (2006) 3075–3080 (2006).
- [78] F. Li, T. Ohkubo, Y. Chen, M. Kodzuka, F. Ye, D. Ou, K. Hono, Laser-assisted three-dimensional atom probe analysis of dopant distribution in gd-doped CeO₂, Scripta Materialia 63 (2010) 332–335 (2010). doi:https://doi.org/10.1016/j.scriptamat.2010.04.029.
- [79] G. Arora, D. S. Aidhy, Segregation and binding energetics at grain boundaries in fluorite oxides, Journal of Materials Chemistry A 5 (2017) 4026– 4035 (2017).
- [80] Ionic radii in crystals.

- $\label{eq:url} URL \qquad \text{https://bionumbers.hms.harvard.edu/files/Ionic\%20Radii\%20in\%20Crystals.pdf}$
- [81] D. A. Andersson, S. I. Simak, N. V. Skorodumova, I. A. Abrikosov, B. Johansson, Optimization of ionic conductivity in doped ceria, Proceedings of the National Academy of Sciences 103 (2006) 3518–3521 (2006).
- [82] S. R. Bishop, T. S. Stefanik, H. L. Tuller, Electrical conductivity and defect equilibria of $Pr_{0.1}Ce_{0.9}O_{2-\delta}$, Physical Chemistry Chemical Physics 13 (21) (2011) 10165–10173 (2011). doi:10.1039/C0CP02920C.
- [83] F. M. L. Figueiredo, F. M. B. Marques, Electrolytes for solid oxide fuel cells, Wiley Interdisciplinary Reviews: Energy and Environment 2 (1) (2013) 52– 72 (2013). doi:10.1002/wene.23. URL http://doi.wiley.com/10.1002/wene.23
- [84] K. Ahn, Y. C. Chung, K. J. Yoon, J. W. Son, B. K. Kim, H. W. Lee, J. H. Lee, Lattice-strain effect on oxygen vacancy formation in gadolinium-doped ceria, Journal of Electroceramics 32 (2014) 72–77 (2014). doi:10.1007/s10832-013-9844-6.
- [85] K. Wen, W. He, Interfacial lattice-strain effects on improving the overall performance of micro-solid oxide fuel cells, Journal of Materials Chemistry A 3 (2015) 20031–20050 (2015). doi:10.1039/c5ta03009a.
- [86] D. S. Aidhy, Y. Zhang, W. J. Weber, Stabilizing nanocrystalline grains in ceramic-oxides, Physical Chemistry Chemical Physics 15 (2013) 18915 (2013). doi:10.1039/c3cp53052c. URL http://xlink.rsc.org/?D0I=c3cp53052c
- [87] T. Bondevik, T. Bjorheim, T. Norby, Assessing common approximations in space charge modeling to estimate the proton resistance across grain boundaries in Y-doped BaZrO₃, Physical Chemistry Chemical Physics 22 (2020). doi:10.1039/c9cp06625j.

[88] D. Wolf, S. Yip, Materials Interfaces: Atomic-Level Structure and Properties, Springer, Netherlands, 1993 (1993).